Available online at www.sciencedirect.com
SCIENCE DIRECT
Earth and Planetary Science Letters 241 (2006) 962–971
EPSL
www.elsevier.com/locate/epsl

QLM9: A new radial quality factor (Q_μ) model for the lower mantle

Jesse F. Lawrence *, Michael E. Wysession

Washington University, USA

Received 26 April 2004; received in revised form 10 October 2005; accepted 10 October 2005
Available online 15 December 2005
Editor: R.D. van der Hilst

Abstract

We employ a niching genetic algorithm to invert ~30,000 differential *ScS/S* attenuation values for a new spherically symmetric radial model of shear quality factor (Q_μ) with high sensitivity to the lower mantle. The new radial Q_μ model, QLM9, possesses greater sensitivity to Q_μ at large mantle depths than previous studies. On average, lower mantle Q_μ increases with depth, which supports models of increasing viscosity with depth [B.M. Steinberger, A.R. Calderwood. Mineral physics constraints on viscous flow models of mantle flow, J. Conf. Abs., 6, 2001., 2001.]. There are two higher-Q_μ regions at ~1000 and ~2500 km depth, which roughly correspond to high-viscosity regions observed by Forte and Mitrovica [A.M. Forte and J.X. Mitrovica, Deep-mantle high-viscosity flow and thermochemical structure inferred from seismic and geodynamic data, Nature 410, 1049–1056, 2001.]. There is a lower-Q_μ layer at the core–mantle boundary and a relatively low-Q_μ region in the mid-lower mantle. With several caveats, we infer a divergence of the solidus and geotherm in the lower mantle and a convergence within D'' by relating Q_μ to homologous temperature.

Keywords: Quality factor; Attenuation; Lower mantle; Body waves

1. Introduction

Attenuation is important for understanding the material properties of the Earth [3]. Yet, the gross radial Q_μ structure is poorly resolved for the lower mantle due to lower sensitivity. Various early models of depth-dependent Q_μ, made with different parameterizations and methods of analysis, are in disagreement [4–8]. Despite significant differences between radial Q_μ models, these models do agree that the asthenosphere is the most attenuating layer within the mantle and that Q_μ generally increases with depth. Quality factor is a key indicator for thermal anomalies. At upper mantle pressures and temperatures, Q_μ can decrease exponentially as the result of temperature increase [9]. In the upper mantle, maps of Q_μ delineate subduction zones and back-arc basins [10,11] as well as spreading ridges [12].

Through differential attenuation measurement (dt^*_{ScS-S}) of over 30,000 *S* and *ScS* phases we create a new radial model of shear quality factor (Q_μ) with high sensitivity to the lower-mantle. In general, the attenuating properties of the lower mantle are difficult to model because the majority of *S* and *ScS* attenuation accumulates in the asthenosphere, dominating the signal from the higher-Q_μ lower mantle. However, because *S* and *ScS* paths are similar in the upper mantle, dt^*_{ScS-S} has better resolution in the lower mantle than the upper mantle (Fig. 1).

In this study, we invert the globally averaged dt^*_{ScS-S} observations with respect to epicentral distance for

* Corresponding author. Tel.: +1 858 822 5979; fax: +1 858 534 5332.
E-mail address: jlawrence@ucsd.edu (J.F. Lawrence).

0012-821X/$ - see front matter © 2005 Elsevier B.V. All rights reserved.
doi:10.1016/j.epsl.2005.10.030

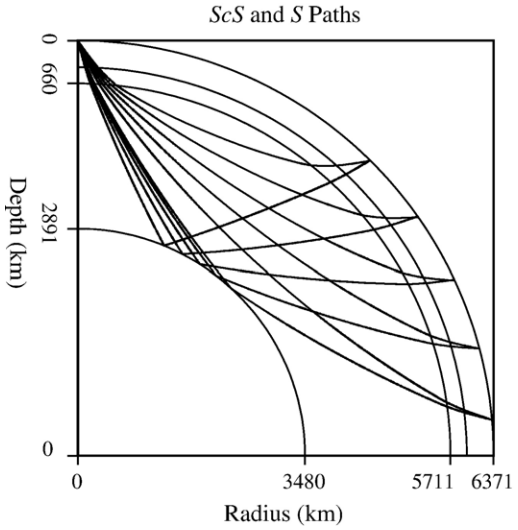

Fig. 1. *ScS* and *S* ray paths through the mantle for distances of 45°, 55°, 65°, 75°, and 85°.

spherically symmetric radial Q_μ models. Using a niching genetic algorithm (NGA) [13], we determine a radial Q_μ model that best fits the observed epicentral variation in dt*. We divide the differential measurements into two categories (shallow and deep events) to determine the best match for shallow and deep events separately and together. The resulting models are less sensitive to upper mantle Q_μ and more sensitive to lower mantle Q_μ than previous models.

2. Attenuation measurements

We used 26,973 shallow source (<100 km) and 3436 deep source (>400 km) event-to-station paths to determine the globally averaged dt^*_{ScS-S} as functions of epicentral distance. We examined over 300,000 tangential broadband records of earthquakes occurring between 1990 and 2001 with sufficient magnitude (M_b>5.8). We required visual confirmation of both the *S* and *ScS* waves. Additionally, data had to have root-mean-squared signal-to-noise ratios greater than 1.5 for both phases and *ScS–S* cross-correlation coefficients greater than 0.8, reducing the number of usable data by a factor of ten. The largest determining factor in data quantity is the event and station distribution. A relatively even percentage of rejections (89–92%) occurred as a function of distance, which suggests random noise, rather than systematic contamination.

Prior to measuring differential attenuation, we remove the instrument response, rotate the horizontal records into the tangential and radial components, and band-pass filter at 0.018–0.2 Hz. We window 40 s around the theoretical PREM arrival time for each phase on the tangential component. A 20% cosine taper is applied and 20 s of padding are added to each series to reduce ringing in the frequency domain.

Using the method of Bhattacharyya and Masters [14], we measure differential *ScS/S* attenuation values ($dt^*_{ScS/S}$) for tangential *ScS* and *S* phase pairs. Due to the similarity between the *ScS* and *S* takeoff angles at the location of the earthquake, the transfer function between the two phases reduces the effects of the source function and upper-mantle Q_μ near the source and receiver. Spectral division between the *ScS* and *S* waveforms estimates the transfer function. Differential attenuation is the negative measure of the log–linear slope for the $ScS(\omega)/S(\omega)$ transfer function between *ScS* and *S* in the amplitude spectrum (Fig. 2). The slope is calculated with a linear inversion that has an associated normalized least squares misfit (ξ), which is a good measurement of the $\delta t^*_{ScS/S}$ uncertainty. After the measurement of $\delta t^*_{ScS/S}$, we attenuate the less-attenuated time series (*S* or *ScS*) by the attenuation operator and cross-correlate the two waves. The post-attenuation cross-correlation coefficient (γ) provides a good measure of both the quality of the data and the suitability of applying the attenuation operator. Only measures with greater correlation coefficients after attenuation (or which remain roughly constant, for the case of negligible differential attenuation) are used.

We divide the attenuation measurements into two subsets because the shallow events travel through the highly attenuating asthenosphere twice, whereas the deep events travel through the asthenosphere only once. We calculate the averaged differential attenuation for nine epicentral distances in the range of 45° to 85°

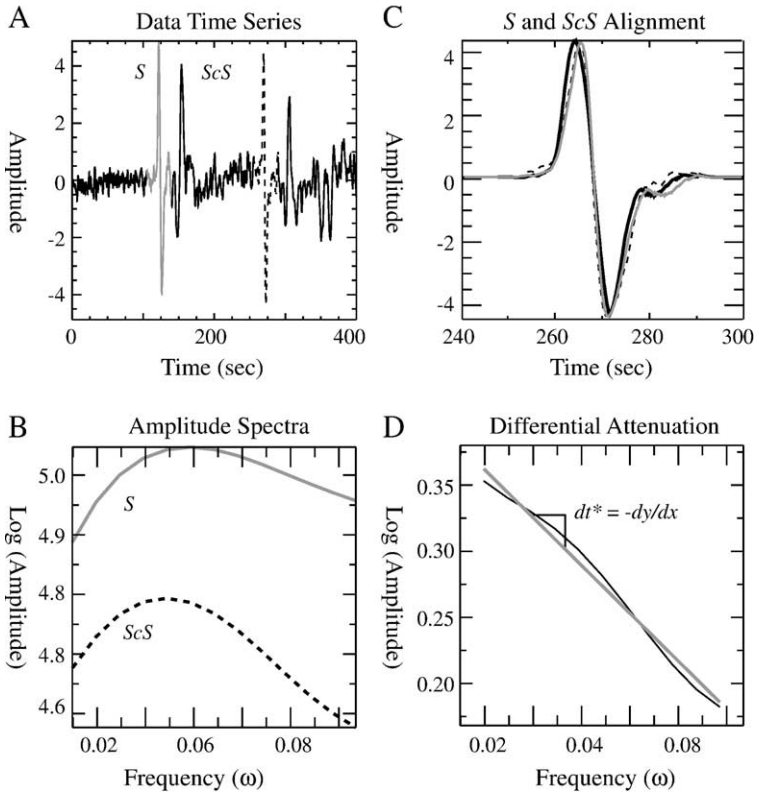

Fig. 2. An example of (A) the *S* and *ScS* data, (B) their smoothed spectra, (C) the *ScS* wave (dashed) aligned with the *S*-wave before (grey) and after (black) applying the attenuation operator, and (D) the differential attenuation measurement.

(Fig. 3). Within this distance range the *S* and *ScS* phases are distinct from each other and other phases such as *SS*, which could possibly interfere with the differential measurement. As the measurement is obtained for the tangential component, waves observed on the radial component, such as *SKS*, are of lesser concern (though anisotropic effects can cause *SKS* arrivals on transverse components).

Each weight-averaged $\delta t^*_{ScS/S}$ value uses all ray paths with epicentral distance within 2.5° of the desired distance, creating bins of 5° at intervals of 5°. Attenuation values are weighted in the average using $w=\gamma/(1+\xi)$. To verify that these averages are statistically significant, we contour the normalized number of data points versus distance and differential attenuation. For all cases, the contour maxima and averaged $\delta t^*_{ScS/S}$

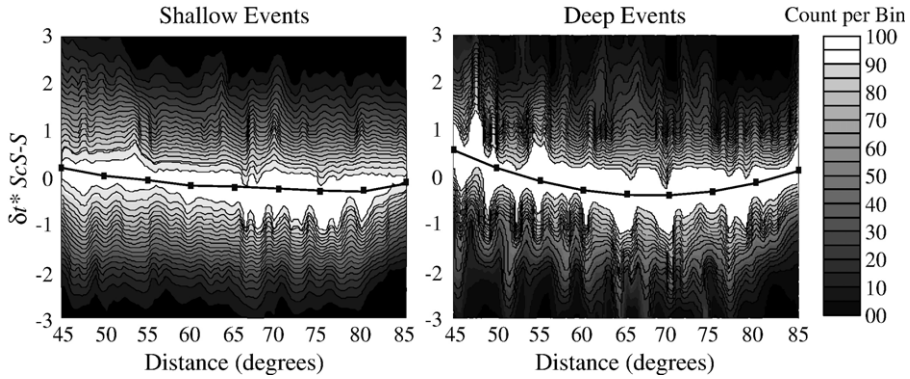

Fig. 3. Average differential *ScS/S* attenuation (heavy line) as a function of epicentral distance overlying a density function contour plot of *ScS/S* attenuation vs. epicentral distance. For each epicentral distance, the attenuation distribution is normalized to unity to remove effects of non-uniform epicentral distance coverage.

values are equivalent, possessing roughly Gaussian distributions around the mean at each value of distance. The standard deviation is large, indicating significant noise and/or lateral structural deviation from a mean radial Q_μ model. The weight-averaged values remain statistically identical for any number of different subsets of both shallow and deep datasets, suggesting that the mean differential attenuation values are robust for each distance range. The shallow and deep event measurements are sufficiently different to warrant separate analysis (Fig. 3).

3. Attenuation modeling

Differential attenuation (dt^*) and quality factor (Q_μ) are related by the equation $dt^* = \sum_1^M (\Delta T_{ScS}(Z_i) - \Delta T_S(Z_i))/Q_\mu(Z_i)$, where ΔT_{Si} and ΔT_{ScSi} are the theoretical PREM S and ScS travel times and $Q_\mu(z)$ is the quality factor for each layer, i, at depth z. We simulate 'inversion' using the niching genetic algorithm (NGA) [13], which uses an evolutionary paradigm of forward modeling to efficiently search the model space for the most optimal solution. The genetic algorithm creates a population of random Q_μ models and then determines the misfit to the observed $dt^*_{ScS/S}$. Models associated with high misfit are removed from the population, while those with low misfit are passed on to further generations. In following iterations new models are created by randomly mutating some parameters of previous low-misfit models in order to provide a more thorough search of the model space. Additional models are constructed by randomly combining the parameters of previous low-misfit models, causing the population to converge toward more optimal solutions. Additionally, models associated with high second-derivative model roughness are penalized with lower probabilities of propagating to further generations, maintaining model smoothness. The NGA is a compound genetic algorithm that requires various subset populations to search separate multidimensional volumes of the model space by penalizing models for similarity. In this manner the NGA converges upon multiple locally optimal models. The most optimal model for all sub-populations is the globally optimal model. While the NGA does not employ a linear inversion, it simulates an inversion and we refer to the process colloquially as an inversion through the remainder of this document.

The niching genetic algorithm has several advantages. First, the NGA locates various model types, demonstrating parameter tradeoffs. Second, the NGA, if working properly, locates the globally optimal solution rather than just a locally optimal solution. Third, the NGA does not depend heavily upon starting model. Instead, the NGA only requires a model space ($60 < Q_{\mu i} < 600$), which reduces the bias provided by a priori information. Larger model spaces were used for several subsets of data. However the best-fit models converged on solutions within this range.

The sensitivity of dt^*_{ScS-S} to Q_μ in any particular layer is proportional to the differential time accumulated in each layer and the change in differential time accumulated in each layer with distance. dt^*_{ScS-S} is largely insensitive to attenuation in the uppermost mantle and crust due to the small differential times accumulated there. When these layers are included in an inversion, the solution space is non-unique. Q_μ values for the top three layers can vary by a factor of two to four in opposite directions without significant alteration of optimal lower mantle structure or data misfit. To provide a more realistic upper mantle Q_μ structure we constrain the Q_μ for the uppermost three layers to that of PREM (down to a depth of 400 km) [5]. Deeper layers accumulate both larger differential travel times and larger variations in travel times (Fig. 1). Consequently, dt^*_{ScS-S} is highly sensitivity to Q_μ in the lower mantle.

The inversion process and data warrant small-scale (~140 km depth spacing) inversion of radial Q_μ in the lower mantle. The largest change in travel time through a layer with distance occurs as a result of the S-wave bottoming within that layer (Fig. 1). By sampling the differential attenuation at 5° intervals, we model S-wave bottoming depths between 950 and 2300 km with an average depth interval of 140 km. The ScS ray path becomes more horizontal at greater depth and at greater distances, giving rise to larger travel times and greater sensitivity in the lowermost mantle.

4. Results

The weight-averaged differential ScS–S attenuation ($\delta t^*_{ScS/S}$) is positive at shorter distances (~45°) indicating more ScS attenuation than S attenuation (Fig. 3). The ScS ray path is much longer at short distances, allowing for much greater accumulation of attenuation (Fig. 1). The $\delta t^*_{ScS/S}$ values decrease from 45° to between 70° and 75°. At ~50° the differential attenuation actually becomes negative, indicating that the S phase is more attenuated than the ScS phase. Accordingly, there must be lower Q_μ along the S path since the ScS path length is longer than the S path length. At longer distances (75–85°) the differential attenuation increases back toward zero because the S and ScS paths converge.

The most optimal solutions located by the NGA for shallow and deep earthquakes jointly and separately

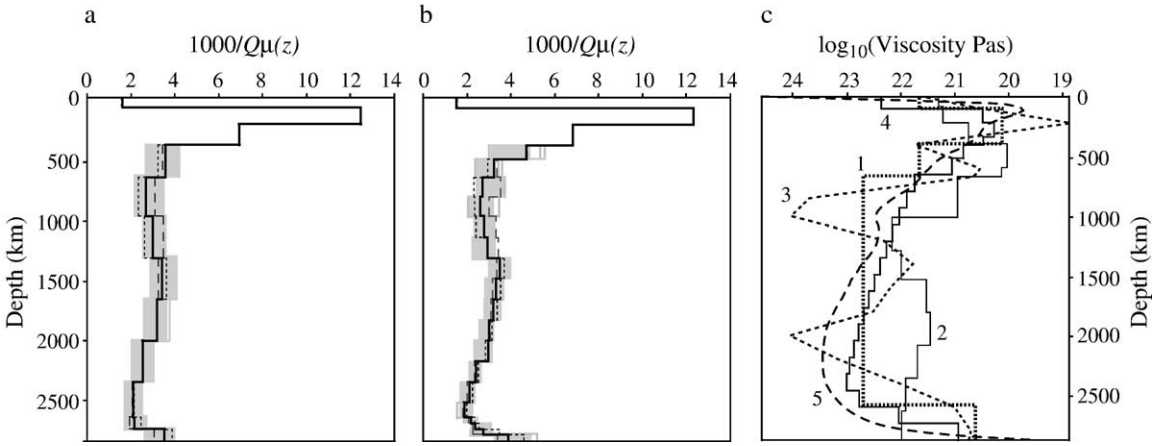

Fig. 4. (a) 12-layer and (b) 21-layer quality factor models produced from NGA inversions using shallow events (dashed), deep events (dotted), and both shallow and deep events (solid). The shaded area represents all models with less than twice the global model's total penalty for the combined shallow and deep event NGA inversion. (c) These quality factor models are similar in varying degrees to viscosity models of (1) Hager and Richards [16], (2) Forte and Mitrovica [2], (3) Forte and Mitrovica [17], (4) Steinberger and Calderwood [1], and (5) McNamara et al. [18].

have strikingly similar Q_μ structures for both 12- and 21-layer models (Fig. 4). Due to the high similarity between resultant models we primarily focus on the simplest model that uses the most data—the 12-layer model that employs both deep and shallow attenuation measurements. The similarity between each of the separate inversions indicates that the Q_μ model is robust. The lower mantle Q_μ is, on average, greater than that of PREM [5], with a low-Q_μ layer at the core–mantle boundary. The quality factor in the uppermost lower mantle is higher than that of PREM. There is a slight decrease in Q_μ toward the mid-mantle, which is statistically indifferent from the PREM values. Toward the lowermost mantle there is a large increase in Q_μ down to ~100 km above the core–mantle boundary. Tradeoff analyses of locally optimal models indicate that upper mantle Q is not well resolved and may be largely influenced by the roughness penalty. The 21-layer model required over twice the roughness penalty required by the 12-layer model to converge upon a reasonably smooth solution. Therefore, we prefer the 12-layer model, QLM9, inverted from both shallow and deep events, which is presented in Table 1. The σ value in Table 1 is the standard deviation for all models associated with less than twice the data misfit of the globally optimal model.

The locally optimal models, which often demonstrate tradeoff in the model space, are largely unstable. These lesser-optimal solutions demonstrate tradeoffs between model roughness and data misfit. Consequently, these models are highly smoothed having poor data fit or possess high data fit with unreasonably rough models. By increasing the acceptable degree of similarity without penalty within the NGA, we located more locally optimal solutions similar to QLM9. Each of the locally optimal models fit within 1 standard deviation of QLM9 (grey area in Fig. 4). In these models the largest stable tradeoff was observed in their fit to shallow and deep event data. Optimal models that better fit the shallow data possessed lower Q_μ at ~1000 km and higher Q_μ in D'' than models that fit the shallow data better. Because this tradeoff is observed within the most optimal solutions for solely deep or shallow event data, these locally optimal solutions are not presented.

The difference between shallow and deep event inversions is smaller than the resolution of the inversion. However, the shallow event inversion consistently requires lower quality factor in the uppermost lower mantle and higher quality factor at the core–mantle boundary (Fig. 4). This difference, if significant, could be a result of choosing PREM Q_μ for the upper-

Table 1

Layer	Q_μ	Depth (km)	Radius (km)	σ
1	600	0–80	6371–6291	–
2	80	80–220	6291–6151	–
3	143	220–400	6151–5971	–
4	276	400–670	5971–5701	18.7
5	362	670–1000	5701–5371	22.4
6	325	1000–1350	5371–5021	14.5
7	287	1350–1700	5021–4671	12.8
8	307	1700–2050	4671–4321	14.7
9	383	2050–2400	4321–3971	19.3
10	459	2400–2700	3971–3671	16.5
11	452	2700–2800	3671–3571	23.1
12	278	2800–2891	3571–3480	17.1

most three layers. PREM overestimates quality factor in the upper mantle compared to other 1D models, such as QM1 [8] and QL6 [4]. Alternatively, the difference may result from geographically different sampling of deep and shallow events. Deep events necessarily are limited to subduction zones, where the Q_μ structure may be different.

5. Discussion

One concern in solving for a 'spherically averaged' 1D radial model is the inability to evenly sample the mantle. The data are not weighted by lateral coverage, so the results are biased by the predominant source-to-receiver path geometries. The deep event data are confined by proximity to subduction zones and the reduced number of events resulting in worse coverage than the shallow event data. However, due to the large lateral distances over which *S* and *ScS* waves travel in the lower mantle, there is sufficient coverage to justify inversion for a 'spherically averaged' radial model (Fig. 5). Nevertheless, the coverage is greater underlying subduction zones, suggesting that QLM9 is more representative of subduction zone regions than other regions. This bias is likely more severe for the structures inverted from deep events. While beyond the scope of this study, the radial average of the preliminary inverted global 3D quality factor structure is very similar to that of QLM9 structure [15].

To first order, the locally and globally optimal solutions from the NGA inversion demonstrate a significant increase in Q_μ with depth in the mantle from the asthenosphere ($Q_\mu \sim 80$) to the bottom of the mantle ($Q_\mu \sim 450$). This is in general agreement with previous results [4–8]. However, in D'', at the very base of the mantle, the mean quality factor decreases sharply ($Q_\mu \sim 275$). To second order, however, there is added complexity to the depth distribution of Q_μ. While the top of the lower mantle displays less attenuation than the overlying upper mantle, the mid-lower-mantle beneath this shows an increase in attenuation, with Q_μ decreasing from 348 to a value of 293 in the mid-lower mantle layer.

Modeling Q_μ with various different radial layer thicknesses leads to approximately similar models. The most significant tradeoff between Q_μ and layer thickness occurs at the core–mantle boundary. The 21-layer model requires that lower Q_μ values concentrate at the core mantle boundary. The 21-layer NGA inversions resulted in a lowermost layer for each data set having a ~20% lower Q_μ than the layer immediately above. The gradual gradient of the 21-layer model indicates that Q_μ decreases sharply, but continuously, near the core–mantle boundary. No layering scheme resulted in a consistent and robust depth for a first-order discontinuous Q_μ interface in D'' or the rest of the lower mantle. However, the vertical resolution (~140 km at best) within the lower mantle may limit the inversion's ability to locate an interface.

PREM overestimates the quality factor of the lithosphere compared to QM1 [8] and QL6 [4], which can bias our model. In Fig. 6, variations of Q_μ from 80 to 600 in the lithosphere cause insubstantial variations in calculated dt^*_{ScS-S} when compared to the variations shown in Fig. 3. This is due to the similarity between the ray paths of the *S* and *ScS* waves in the upper mantle. Significant variations from PREM in the other two fixed layers cause slightly more substantial changes in dt^*, but even these variations are insignificant compared with lower mantle structure. PREM Q_μ

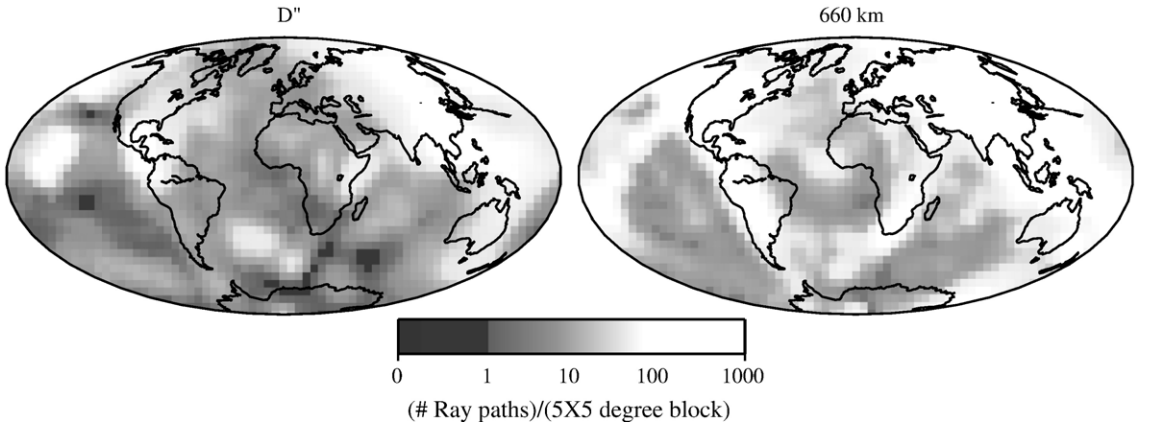

Fig. 5. The respective lateral ray path counts through D'' and the 660-km discontinuity for each $5^\circ \times 5^\circ$ region demonstrate good global coverage with emphasis underlying subduction zones.

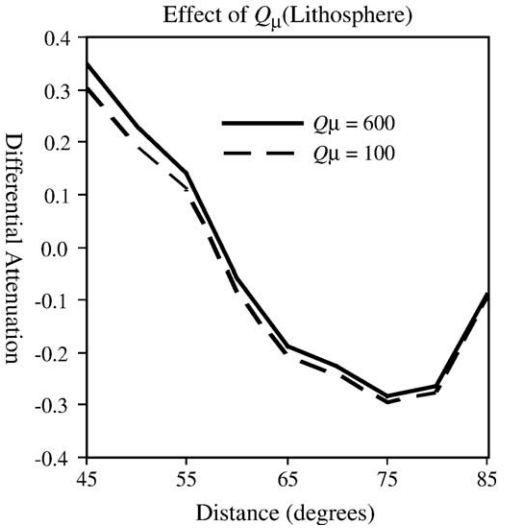

Fig. 6. Variations of Q_μ of 80 and 600 for the lithosphere cause little variation in the resulting differential *ScS–S* attenuation.

for the asthenosphere and deep upper mantle is much more similar to QL6 and QM1 than the lithosphere (Fig. 7). Therefore, the need to account for differences between these layers is much less. Consequently we find that the bias of fixing the upper most three layers is not significant.

Between 400 and ~1500 km depth QLM9 is very similar to QM1 [8], with Q_μ first increasing to a depth of ~1000 km, and then decreasing to a depth of 1500 km (Fig. 7). The other two models compared here (PREM [5] and QL6 [4]) have constant Q_μ below the 660 km discontinuity. Between depths of 660 and 2000 km, QLM9 is roughly bound by PREM and QL6. Below ~2000 km none of these models agree. QLM9 has a significantly higher Q_μ between 2000 km and D'', while QM1 has significantly lower values than either QL6 or PREM. Prior to inverting a block model for QM1, Widmer et al. [8] resolved a boxcar-like averaging function inversion of Q_μ structure similar to QLM9 that was rejected on the basis of poor resolution of Q_κ in the core. We propose that this alternate model may be the better estimate of mantle Q_μ structure. The theoretical *ScS–S* differential attenuation as a function of distance calculated from these various models is significantly different (Fig. 7.b). Table 2 demonstrates that QLM9 decreases χ^2 by two to four orders of magnitude over other models.

Table 2

Model	χ^2
QLM9	0.4
QL6	6.1
PREM	23
QM1	45

Differences between previous 1D models and QLM9 may result from several significant factors. First, the parameterizations of these inversions are highly influential upon the outcome. The parameterization of QL6 and PREM are indicative of the second factor; surface wave and normal mode decay have decreased sensitivity to lower mantle quality factor structure compared to upper mantle structure. Third, as noted above, this model is weighted toward subduction zone structure due to uneven lateral sampling, which may bias the results. Fourth, quality factor may not be constant over the periods spanned between this and other studies ($5 < T < 300$ s).

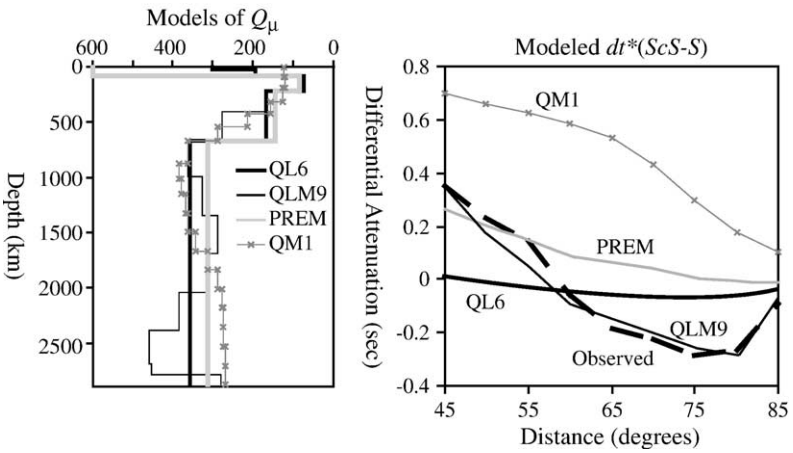

Fig. 7. QLM9 (black thin) agrees well with QM1 (crosses), QL6 (black thick), and PREM (grey thick) in the uppermost mantle. QLM9 deviates from these models in the lowermost mantle. These model differences give rise to significantly different *ScS–S* differential attenuation vs. distance curves for shallow events. QLM9 best matches the observed weight-averaged values as a function of distance (dashed).

The quality factor is dependent upon the effects of pressure and temperature and chemical composition. Regardless of the cause—chemical or thermal—the changes in lowermost mantle Q_μ with depth are likely accompanied by changes in viscosity. Temperature-dependent viscosity and quality factor are both anelastic responses to stresses within the Earth and likely proportional to homologous temperature with an Arrhenius-type relation. At the most limited resolution of the lower mantle, the results agree with Hager and Richards [16], which indicates a low viscosity layer at the base of the mantle. The increase in Q_μ with depth across the lower mantle is in agreement with viscosity models such as Steinberger and Calderwood [1]. QLM9 has two high-Q_μ layers at depths of ~1000 and ~2500 km, which roughly correspond to the depths of the high viscosity layers found by Forte and Mitrovica [2,17]. QLM9 is also similar to the log-averaged viscosity from heterogeneous convection models of McNamara et al. [18], indicating that either the averaging of heterogeneous structures is partially responsible for the shape of QLM9 or that both dislocation and diffusion creep are important factors in lower mantle anelasticity.

If changes in Q_μ provide an accurate assessment of changes in viscosity, then the high viscosity of the lower mantle (inferred from QLM9) may impede low viscosity D'' material from rising [19]. Decreased viscosity within D'' may increase small-scale convection at the base of the mantle [20], accounting for small-scale features observed using temporary seismic arrays [21]. A deep peak in viscosity (similar to the Q_μ peak) is expected above D'' as a result of pressure and temperature dependence [22]. An increased viscosity between 660 and ~1400 km might impede transfer of material between the upper and lower mantle. Alternatively, viscosity could increase at ~1000 km as a result of slab accumulation [23], and a decrease in viscosity in the mid-mantle (~1500 km) could simply reflect the fact that subducting lithosphere may travel more quickly across this depth before accumulating in the deeper mantle, akin to a mantle avalanche model (e.g. [33]). When the relationships between seismic attenuation and viscosity become better understood, models of mantle attenuation like the one presented here will provide important constraints on the style and modes of mantle convection.

An Arrhenius exponential relationship between quality factor and homologous temperature, $T_H(z)$, is likely [9,24]. While the actual temperature (geotherm) increases with depth, which would cause a decrease in Q_μ, so does the melting temperature (solidus), which would tend to increase Q_μ. Due to the complexity of high-pressure mineral physics measurements, the pressure and temperature dependencies of Q_μ are ill-constrained for the suite of minerals, pressures, and temperatures possible in the lower mantle. Therefore, it is currently impossible to directly relate homologous temperature to radial quality factor.

So, with some caveats we calculate a least-squares fit for a depth-independent Arrhenius exponential relationship of upper- and mid-mantle Q_μ [9] and homologous temperature [25], and extrapolate this relation into the lower mantle. The Arrhenius relationship ($Q_\mu(z)=\alpha e^{[\beta/TH(z)]}$) was best fit to the temperature profile of Stacy [25] and QLM9 with parameters $\alpha=2.14\pm1$ and $\beta=3.45\pm0.6$. While other relationships are equally as valid, we choose this empirically derived relationship to showcase how our model is consistent with the geodynamics of the lower mantle. This relationship spans over three major phases corresponding to the transition zones (220 and 410) and a depth range of 100 to 600 km. Consequently the resulting relationship accounts for phase changes and pressure dependence. The appropriateness of this extrapolation depends upon the similarity between upper and lower mantle bulk composition, thermal expansion, activation energy, and phase changes. The empirically derived relationship falls within the bounds of the mineral physics measurements of Getting et al. [26], and Webb et al. [27]. Using a different Q_μ model for the upper mantle significantly changes the resulting fit, but not the overarching pattern of results inferred from the fit.

We use the Arrhenius relationship to estimate a hypothetical radial homologous temperature profile from QLM9 (Fig. 8). We display the homologous temperature on a non-dimensional plot to emphasize that the actual values are ill-constrained, but the trends may be valid. The inferred homologous temperature has two lows at depths of ~1000 and ~2500 km, which correspond to the depths of the high-Q_μ layers. We can non-uniquely interpret a radial change in homologous temperature as a change in either the geotherm or solidus. We infer several characteristics about the temperature profile from the calculated homologous temperature profile (Fig. 8). On average, the gradient of the geotherm is less than the gradient of the solidus for the lower mantle. The most rapid variation in lower mantle temperature gradients occurs near the core–mantle boundary. These general results are relatively uniform regardless of the chosen Arrhenius relationship. If we assume little to no change in the lower mantle solidus gradient, then the geotherm has the

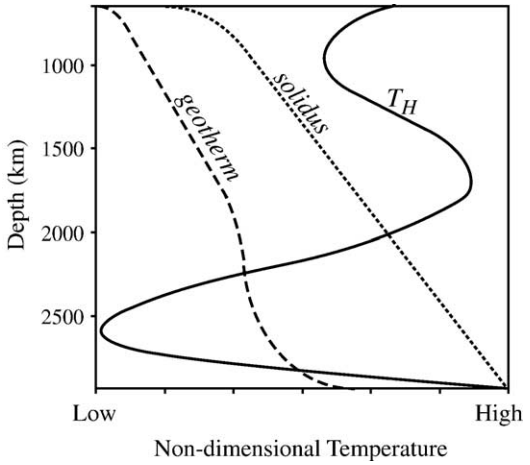

Fig. 8. By relating the Q_μ model QLM9 to homologous temperature using an Arrhenius relationship, we calculate a non-dimensional homologous temperature profile (solid line). We calculate a non-dimensional geotherm (dashed) from a smooth, non-dimensional solidus (dotted) and the homologous temperature profile.

approximate shape of an error function near the core–mantle boundary. This is expected for a thermal boundary layer [28] across which heat is conducting from the core. Nevertheless, the non-unique nature of homologous temperature does not exclude a change in the gradient of the solidus at the core–mantle boundary due iron or volatile enrichment [29], chemical variation, or other processes.

The attenuation measurements used here to determine quality factor might be influenced by anisotropy, scattering, and elastic responses to layering. These contributions to attenuation likely alter the shape of our optimized quality factor models. There is a correlation between attenuation and anisotropy anomalies [30], indicating that the same physical process that causes anisotropy, or anisotropy itself, may influence attenuation. Scattering, due to elastic small-scale structures observed within D'' [21,31] and in the upper mantle [10,12], may alter dt^*_{ScS-S}. The contribution of scattering to seismic attenuation throughout the mantle remains a concern for addressing the thermochemical implications of our results. However, the exponential relationship between differential attenuation and travel-time anomalies found in the lower mantle beneath Central America also suggests that the attenuation may be due to thermal anomalies [32]. If the influence of layering is significant, then the waveform shape would be altered significantly, causing low correlation and exclusion from this study. In the future, 3D Q_μ measurements of the lower mantle may better correlate quality factor with anisotropy, seismic velocity, and/or bulk to shear velocity ratios [32].

6. Conclusion

Differential *ScS–S* attenuation as a function of event-to-station distance provides an excellent mechanism for determining lower mantle quality factor structure regardless of upper mantle structure. A new 1D lower mantle quality factor model, QLM9, based upon *ScS–S* attenuation, shows increasing lower mantle quality factor with depth. At D'' the quality factor increases with proximity to the core–mantle boundary. This model is robust for both shallow and deep event data sets. QLM9, when compared to viscosity and temperature (with significant caveats), is in agreement with geodynamic expectations.

Acknowledgements

Thanks to input from Shun Karato, the interpretation of this document was greatly improved. The faculty and staff at Scripps IGPP are thanked for providing space and facilities for the writing of this manuscript. We also thank the reviewers, Barbara Romanowicz and Joe Durek for their contributions. This project was funded under NSF grants EAR-9903260, EAR-0207737, and EAR-0207751.

References

[1] B.M. Steinberger, A.R. Calderwood, Mineral physics constraints on viscous flow models of mantle flow, J. Conf. Abstr. 6 (2001) 2001.
[2] A.M. Forte, J.X. Mitrovica, Deep-mantle high-viscosity flow and thermochemical structure inferred from seismic and geodynamic data, Nature 410 (2001) 1049–1056.
[3] S. Karato, Importance of anelasticity in the interpretation of seismic tomography, Geophys. Res. Lett. 20 (1993) 1623–1626.
[4] J.J. Durek, G. Ekstrom, A radial model of anelasticity consistent with long period surface wave attenuation, Bull. Seismol. Soc. Am. 86 (1A) (1996) 144–158.
[5] A.M. Dziewonski, D.L. Anderson, Preliminary reference Earth model, Phys. Earth Planet. Inter. 25 (1981) 297–356.
[6] D.L. Anderson, R.S. Hart, Attenuation models of the Earth, Phys. Earth Planet. Inter. 16 (1978) 289–306.
[7] G. Masters, F. Gilbert, Attenuation in the Earth at low frequencies, Philos. Trans. R. Soc. Lond. A308 (1983) 479–522.
[8] R. Widmer, G. Masters, F. Gilbert, Spherically symmetric attenuation within the Earth from normal mode data, Geophys. J. Int. 104 (1991) 541–553.
[9] B. Romanowicz, A global tomographic model of shear attenuation in the upper mantle, J. Geophys. Res. 100 (B7) (1995) 12,375–12,394.
[10] E.G. Roth, D.A. Wiens, D. Zhao, An empirical relationship between seismic attenuation and velocity anomalies in the upper mantle, Geophys. Res. Lett. 27 (5) (2000) 601–604.
[11] Y. Gung, B. Romanowicz, *Q* tomography of the upper mantle using three component long-period waveforms, Geophys. J. Int. 157 (2004) 813–830.

[12] M.P. Flanagan, D.A. Wiens, Radial upper mantle attenuation structure of inactive back arc basin differential shear wave measurements, J. Geophys. Res. 99 (B8) (1994) 15,469–15,485.
[13] K.D. Koper, M.E. Wysession, D.A. Wiens, Multimodal function optimization with a niching genetic algorithm: a seismological example, Bull. Seismol. Soc. Am. 89 (4) (1999) 978–988.
[14] J. Bhattacharyya, G. Masters, Global lateral variation of shear wave attenuation in the upper mantle, J. Geophys. Res. 101 (B10) (1996) 22273–22287.
[15] J.F., Lawrence, M.E., Wysession, VQM3DA: a 3D whole-mantle velocity, anisotropy, and quality factor model. In preparation, 2004, G3 (in preparation).
[16] B.H. Hager, M.A. Richards, Long-wavelength variations in Earth's geoid: physical models and dynamical implications, Philos. Trans. R. Soc. Lond A328 (1989) 309–327.
[17] A.M. Forte, J.X. Mitrovica, New inferences of mantle viscosity from joint inversion of long-wavelength mantle convection and post-glacial rebound data, Geophys. Res. Lett. 23 (1996) 1147–1150.
[18] A.K. McNamara, P.E. van Keken, S. Karato, Development of finite strain in the convecting lower mantle and its implications for seismic anisotropy, J. Geophys. Res. 108 (2003), doi:10.1029/2002JB001970.
[19] L.H. Kellogg, S.D. King, Effect of mantle plumes on the growth of D by reaction between the core and mantle, Geophys. Res. Lett. 20 (1993) 379–382.
[20] V.S. Solomatov, L. Moresi, Small-scale convection in the D″ layer, J. Geophys. Res 107 (2002), doi:10.1029/2000JB000063.
[21] S. Russell, T. Lay, E.J. Garnero, Seismic evidence for small-scale dynamics in the lower most mantle at the root of the Hawaiian hotspot, Nature 396 (1998) 255–258.
[22] P.E. van Keken, D.A. Yuen, A.P. van der Berg, Implications for mantle dynamics from the high melting temperature of perovskite, Science 264 (1994) 1437–1439.
[23] M. Grand, H. Shiobara, T. Janik, A. Guterch, H. Shimamura, Crustal model of the Bransfield Rift, West Antarctica, from detailed OBS refraction experiments, Geophys. J. Int. 130 (1997) 506–518.
[24] H. Sato, S. Sacks, T. Murase, G. Muncill, H. Fukuyama, Qp-melting temperature relation in peridotite at high pressure and temperature: attenuation mechanism and implications for the mechanical properties of the upper mantle, J. Geophys. Res. 94 (B8) (1989) 10,647–10,661.
[25] F.D. Stacey, Physics of the Earth, Brookfield Press, Brisbane, 1992, 513 pp.
[26] I.C. Getting, S.J. Dutton, P.C. Burnley, S. Karato, H.A. Spetzler, Shear attenuation and dispersion in MgO, Phys. Earth Planet. Inter. 99 (1997) 249–257.
[27] S. Webb, I. Jackson, J. Fitz Gerald, Viscoelasticity of the titanate perovskites $CaTiO_3$ and $SrTiO_3$ at high temperature, Phys. Earth Planet. Inter. 115 (1999) 259–291.
[28] D.L. Turcotte, G. Schubert, Geodynamics: Applications of Continuum Physics to Geological Problems, Wiley, New York, 1982.
[29] E. Knittle, R. Jeanloz, Earth's core–mantle boundary: results of experiments at high pressure and temperature, Science 251 (1991) 1438–1443.
[30] T.R. Portle, J.F. Lawrence, M.E. Wysession, Global lower mantle velocity, attenuation, and anisotropy from differential ScS–*S* analyses, EOS Trans. AGU Fall Suppl. 84 (46) (2003) (Abstract U41C-05).
[31] V.F. Cormier, D″ as a transition in the heterogeneity spectrum of the lowermost mantle, J. Geophys. Res. 105 (2000) 16193–16205.
[32] J.L. Fisher, M.E. Wysession, K.M. Fischer, Small-scale lateral variations in D″ attenuation and velocity structure, Geophys. Res. Lett. 30 (2003), doi:10.1029/2002GL016179.
[33] P. Machetel, P. Weber, Intermittent layered convection in a model mantle with an endothermic phase change at 670 km, Nature 350 (1991) 55–57.